

Measurement of attenuation length of the muon content in extensive air showers from 0.3 to 30 PeV with LHAASO

Zhen Cao,^{1,2,3} F. Aharonian,^{4,5} Axikegu,⁶ Y.X. Bai,^{1,3} Y.W. Bao,⁷ D. Bastieri,⁸ X.J. Bi,^{1,2,3} Y.J. Bi,^{1,3} W. Bian,⁹ A.V. Bukevich,¹⁰ Q. Cao,¹¹ W.Y. Cao,^{13,12} Zhe Cao,^{13,12} J. Chang,¹⁴ J.F. Chang,^{1,3,13} A.M. Chen,⁹ E.S. Chen,^{1,2,3} H.X. Chen,¹⁵ Liang Chen,¹⁶ Lin Chen,⁶ Long Chen,⁶ M.J. Chen,^{1,3} M.L. Chen,^{1,3,13} Q.H. Chen,⁶ S. Chen,¹⁷ S.H. Chen,^{1,2,3} S.Z. Chen,^{1,3} T.L. Chen,¹⁸ Y. Chen,⁷ N. Cheng,^{1,3} Y.D. Cheng,^{1,2,3} M.C. Chu,¹⁹ M.Y. Cui,¹⁴ S.W. Cui,¹¹ X.H. Cui,²⁰ Y.D. Cui,²¹ B.Z. Dai,¹⁷ H.L. Dai,^{1,3,13} Z.G. Dai,¹² Danzengluobu,¹⁸ X.Q. Dong,^{1,2,3} K.K. Duan,¹⁴ J.H. Fan,⁸ Y.Z. Fan,¹⁴ J. Fang,¹⁷ J.H. Fang,¹⁵ K. Fang,^{1,3} C.F. Feng,²² H. Feng,¹ L. Feng,¹⁴ S.H. Feng,^{1,3} X.T. Feng,²² Y. Feng,¹⁵ Y.L. Feng,¹⁸ S. Gabici,²³ B. Gao,^{1,3} C.D. Gao,²² Q. Gao,¹⁸ W. Gao,^{1,3} W.K. Gao,^{1,2,3} M.M. Ge,¹⁷ T.T. Ge,²¹ L.S. Geng,^{1,3} G. Giacinti,⁹ G.H. Gong,²⁴ Q.B. Gou,^{1,3} M.H. Gu,^{1,3,13} F.L. Guo,¹⁶ J. Guo,²⁴ X.L. Guo,⁶ Y.Q. Guo,^{1,3} Y.Y. Guo,¹⁴ Y.A. Han,²⁵ O.A. Hannuksela,¹⁹ M. Hasan,^{1,2,3} H.H. He,^{1,2,3} H.N. He,¹⁴ J.Y. He,¹⁴ Y. He,⁶ Y.K. Hor,²¹ B.W. Hou,^{1,2,3} C. Hou,^{1,3} X. Hou,²⁶ H.B. Hu,^{1,2,3} Q. Hu,^{12,14} S.C. Hu,^{1,3,27} C. Huang,⁷ D.H. Huang,⁶ T.Q. Huang,^{1,3} W.J. Huang,²¹ X.T. Huang,²² X.Y. Huang,¹⁴ Y. Huang,^{1,2,3} Y.Y. Huang,⁷ X.L. Ji,^{1,3,13} H.Y. Jia,⁶ K. Jia,²² H.B. Jiang,^{1,3} K. Jiang,^{13,12} X.W. Jiang,^{1,3} Z.J. Jiang,¹⁷ M. Jin,⁶ M.M. Kang,²⁸ I. Karpikov,¹⁰ D. Khangulyan,^{1,3} D. Kuleshov,¹⁰ K. Kurinov,¹⁰ B.B. Li,¹¹ C.M. Li,⁷ Cheng Li,^{13,12} Cong Li,^{1,3} D. Li,^{1,2,3} F. Li,^{1,3,13} H.B. Li,^{1,3} H.C. Li,^{1,3} Jian Li,¹² Jie Li,^{1,3,13} K. Li,^{1,3} S.D. Li,^{16,2} W.L. Li,²² W.L. Li,⁹ X.R. Li,^{1,3} Xin Li,^{13,12} Y.Z. Li,^{1,2,3} Zhe Li,^{1,3} Zhuo Li,²⁹ E.W. Liang,³⁰ Y.F. Liang,³⁰ S.J. Lin,²¹ B. Liu,¹² C. Liu,^{1,3} D. Liu,²² D.B. Liu,⁹ H. Liu,⁶ H.D. Liu,²⁵ J. Liu,^{1,3} J.L. Liu,^{1,3} M.Y. Liu,¹⁸ R.Y. Liu,⁷ S.M. Liu,⁶ W. Liu,^{1,3} Y. Liu,⁸ Y.N. Liu,²⁴ Q. Luo,²¹ Y. Luo,⁹ H.K. Lv,^{1,3} B.Q. Ma,²⁹ L.L. Ma,^{1,3} X.H. Ma,^{1,3} J.R. Mao,²⁶ Z. Min,^{1,3} W. Mitthumsiri,³¹ H.J. Mu,²⁵ Y.C. Nan,^{1,3} A. Neronov,²³ K.C.Y. Ng,¹⁹ L.J. Ou,⁸ P. Pattarakijwanich,³¹ Z.Y. Pei,⁸ J.C. Qi,^{1,2,3} M.Y. Qi,^{1,3} B.Q. Qiao,^{1,3} J.J. Qin,¹² A. Raza,^{1,2,3} D. Ruffolo,³¹ A. Sáiz,³¹ M. Saeed,^{1,2,3} D. Semikoz,²³ L. Shao,¹¹ O. Shchegolev,^{10,32} X.D. Sheng,^{1,3} F.W. Shu,³³ H.C. Song,²⁹ Yu.V. Stenkin,^{10,32} V. Stepanov,¹⁰ Y. Su,¹⁴ D.X. Sun,^{12,14} Q.N. Sun,⁶ X.N. Sun,³⁰ Z.B. Sun,³⁴ J. Takata,³⁵ P.H.T. Tam,²¹ Q.W. Tang,³³ R. Tang,⁹ Z.B. Tang,^{13,12} W.W. Tian,^{2,20} L.H. Wan,²¹ C. Wang,³⁴ C.B. Wang,⁶ G.W. Wang,¹² H.G. Wang,⁸ H.H. Wang,²¹ J.C. Wang,²⁶ Kai Wang,⁷ Kai Wang,³⁵ L.P. Wang,^{1,2,3} L.Y. Wang,^{1,3} P.H. Wang,⁶ R. Wang,²² W. Wang,²¹ X.G. Wang,³⁰ X.Y. Wang,⁷ Y. Wang,⁶ Y.D. Wang,^{1,3} Y.J. Wang,^{1,3} Z.H. Wang,²⁸ Z.X. Wang,¹⁷ Zhen Wang,⁹ Zheng Wang,^{1,3,13} D.M. Wei,¹⁴ J.J. Wei,¹⁴ Y.J. Wei,^{1,2,3} T. Wen,¹⁷ C.Y. Wu,^{1,3} H.R. Wu,^{1,3} Q.W. Wu,³⁵ S. Wu,^{1,3} X.F. Wu,¹⁴ Y.S. Wu,¹² S.Q. Xi,^{1,3} J. Xia,^{12,14} G.M. Xiang,^{16,2} D.X. Xiao,¹¹ G. Xiao,^{1,3} Y.L. Xin,⁶ Y. Xing,¹⁶ D.R. Xiong,²⁶ Z. Xiong,^{1,2,3} D.L. Xu,⁹ R.F. Xu,^{1,2,3} R.X. Xu,²⁹ W.L. Xu,²⁸ L. Xue,²² D.H. Yan,¹⁷ J.Z. Yan,¹⁴ T. Yan,^{1,3} C.W. Yang,²⁸ C.Y. Yang,²⁶ F. Yang,¹¹ F.F. Yang,^{1,3,13} L.L. Yang,²¹ M.J. Yang,^{1,3} R.Z. Yang,¹² W.X. Yang,⁸ Y.H. Yao,^{1,3} Z.G. Yao,^{1,3} L.Q. Yin,^{1,3} N. Yin,²² X.H. You,^{1,3} Z.Y. You,^{1,3} Y.H. Yu,¹² Q. Yuan,¹⁴ H. Yue,^{1,2,3} H.D. Zeng,¹⁴ T.X. Zeng,^{1,3,13} W. Zeng,¹⁷ M. Zha,^{1,3} B.B. Zhang,⁷ F. Zhang,⁶ H. Zhang,⁹ H.M. Zhang,⁷ H.Y. Zhang,¹⁷ J.L. Zhang,²⁰ Li Zhang,¹⁷ P.F. Zhang,¹⁷ P.P. Zhang,^{12,14} R. Zhang,¹⁴ S.B. Zhang,^{2,20} S.R. Zhang,¹¹ S.S. Zhang,^{1,3} X. Zhang,⁷ X.P. Zhang,^{1,3} Y.F. Zhang,⁶ Yi Zhang,^{1,14} Yong Zhang,^{1,3} B. Zhao,⁶ J. Zhao,^{1,3} L. Zhao,^{13,12} L.Z. Zhao,¹¹ S.P. Zhao,¹⁴ X.H. Zhao,²⁶ F. Zheng,³⁴ W.J. Zhong,⁷ B. Zhou,^{1,3} H. Zhou,⁹ J.N. Zhou,¹⁶ M. Zhou,³³ P. Zhou,⁷ R. Zhou,²⁸ X.X. Zhou,^{1,2,3} X.X. Zhou,⁶ B.Y. Zhu,^{12,14} C.G. Zhu,²² F.R. Zhu,⁶ H. Zhu,²⁰ K.J. Zhu,^{1,2,3,13} Y.C. Zou,³⁵ and X. Zuo^{1,3}

(The LHAASO Collaboration)*

¹Key Laboratory of Particle Astrophysics & Experimental Physics Division & Computing Center, Institute of High Energy Physics, Chinese Academy of Sciences, 100049 Beijing, China

²University of Chinese Academy of Sciences, 100049 Beijing, China

³TIANFU Cosmic Ray Research Center, Chengdu, Sichuan, China

⁴Dublin Institute for Advanced Studies, 31 Fitzwilliam Place, 2 Dublin, Ireland

⁵Max-Planck-Institut für Nuclear Physics, P.O. Box 103980, 69029 Heidelberg, Germany

⁶School of Physical Science and Technology & School of Information Science and Technology, Southwest Jiaotong University, 610031 Chengdu, Sichuan, China

⁷School of Astronomy and Space Science, Nanjing University, 210023 Nanjing, Jiangsu, China

⁸Center for Astrophysics, Guangzhou University, 510006 Guangzhou, Guangdong, China

⁹Tsung-Dao Lee Institute & School of Physics and Astronomy, Shanghai Jiao Tong University, 200240 Shanghai, China

¹⁰Institute for Nuclear Research of Russian Academy of Sciences, 117312 Moscow, Russia

¹¹Hebei Normal University, 050024 Shijiazhuang, Hebei, China

¹²University of Science and Technology of China, 230026 Hefei, Anhui, China

¹³State Key Laboratory of Particle Detection and Electronics, China

¹⁴Key Laboratory of Dark Matter and Space Astronomy & Key Laboratory of Radio Astronomy, Purple Mountain Observatory, Chinese Academy of Sciences, 210023 Nanjing, Jiangsu, China

¹⁵Research Center for Astronomical Computing, Zhejiang Laboratory, 311121 Hangzhou, Zhejiang, China

¹⁶Key Laboratory for Research in Galaxies and Cosmology, Shanghai Astronomical Observatory, Chinese Academy of Sciences, 200030 Shanghai, China

¹⁷School of Physics and Astronomy, Yunnan University, 650091 Kunming, Yunnan, China

- ¹⁸Key Laboratory of Cosmic Rays (Tibet University),
Ministry of Education, 850000 Lhasa, Tibet, China
- ¹⁹Department of Physics, The Chinese University of Hong Kong, Shatin, New Territories, Hong Kong, China
- ²⁰Key Laboratory of Radio Astronomy and Technology,
National Astronomical Observatories, Chinese Academy of Sciences, 100101 Beijing, China
- ²¹School of Physics and Astronomy (Zhuhai) & School of Physics (Guangzhou)
& Sino-French Institute of Nuclear Engineering and Technology (Zhuhai),
Sun Yat-sen University, 519000 Zhuhai & 510275 Guangzhou, Guangdong, China
- ²²Institute of Frontier and Interdisciplinary Science,
Shandong University, 266237 Qingdao, Shandong, China
- ²³APC, Université Paris Cité, CNRS/IN2P3, CEA/IRFU, Observatoire de Paris, 119 75205 Paris, France
- ²⁴Department of Engineering Physics & Department of Astronomy, Tsinghua University, 100084 Beijing, China
- ²⁵School of Physics and Microelectronics, Zhengzhou University, 450001 Zhengzhou, Henan, China
- ²⁶Yunnan Observatories, Chinese Academy of Sciences, 650216 Kunming, Yunnan, China
- ²⁷China Center of Advanced Science and Technology, Beijing 100190, China
- ²⁸College of Physics, Sichuan University, 610065 Chengdu, Sichuan, China
- ²⁹School of Physics, Peking University, 100871 Beijing, China
- ³⁰Guangxi Key Laboratory for Relativistic Astrophysics,
School of Physical Science and Technology, Guangxi University, 530004 Nanning, Guangxi, China
- ³¹Department of Physics, Faculty of Science, Mahidol University, Bangkok 10400, Thailand
- ³²Moscow Institute of Physics and Technology, 141700 Moscow, Russia
- ³³Center for Relativistic Astrophysics and High Energy Physics,
School of Physics and Materials Science & Institute of Space Science and Technology,
Nanchang University, 330031 Nanchang, Jiangxi, China
- ³⁴National Space Science Center, Chinese Academy of Sciences, 100190 Beijing, China
- ³⁵School of Physics, Huazhong University of Science and Technology, Wuhan 430074, Hubei, China
- (Dated: October 21, 2024)

The attenuation length of the muon content in extensive air showers provides important information regarding the generation and development of air showers. This information can be used not only to improve the description of such showers but also to test fundamental models of hadronic interactions. Using data from the LHAASO-KM2A experiment, the development of the muon content in high-energy air showers was studied. The attenuation length of muon content in the air showers was measured from experimental data in the energy range from 0.3 to 30 PeV using the constant intensity cut method. By comparing the attenuation length of the muon content with predictions from high-energy hadronic interaction models (QGSJET-II-04, SIBYLL 2.3d, and EPOS-LHC), it is evident that LHAASO results are significantly shorter than those predicted by the first two models (QGSJET-II-04 and SIBYLL 2.3d) but relatively close to those predicted by the third model (EPOS-LHC). Thus, the LHAASO data favor the EPOS-LHC model over the other two models. The three interaction models confirmed an increasing trend in the attenuation length as the cosmic-ray energy increases.

I. INTRODUCTION

In recent years, considerable attention has been paid to the disparities between theoretical models for extensive air shower (EAS) development implemented in Monte Carlo (MC) simulations and observations made in EAS experiments. These differences are crucial indicators for improving theoretical models.

In cosmic-ray air showers, muons are generated through the decay of π and K mesons ($\pi^\pm \rightarrow \mu^\pm + \nu_\mu(\bar{\nu}_\mu)$, $K^\pm \rightarrow \mu^\pm + \nu_\mu(\bar{\nu}_\mu)$) generated in hadronic collisions in the early stages of an EAS. Muons possess high penetration capabilities and preserve crucial information about hadronic interactions at very high energies. Therefore, the muon content of an air shower and its attenuation length are sensitive indicators for validating hadronic interaction models.

The Pierre Auger Observatory has observed an excess of muon content in air showers with primary energy ranging from 6 to 16 EeV, which is higher than that predicted using LHC-tuned hadronic models [1]. This excess muon content within the same energy range was also confirmed by the Telescope Array (TA) experiment, which is the largest experiment conducted in the Northern Hemisphere [2]. Additionally, measurements conducted by the Sydney University Giant Air-shower Recorder (SUGAR), using a muon detector (MD), have shown an increasing excess of muons starting from 0.1 EeV and continuing with increasing primary energy [3]. In contrast, IceTop reported smaller muon densities than the post-LHC model predictions for energies ranging from 1 to 100 PeV [4]. The KASCADE-Grande observatory has also measured the attenuation length of the muon content of air showers at sea level for energies between 20 and 100 PeV and found that it is underestimated by all high-energy hadronic interaction models currently available [5]. Therefore, it can be concluded that none of the post-LHC high-energy hadronic interaction models can consistently describe the evolution of muon content in EASs in the aforementioned energy regime.

* fengxt@mail.sdu.edu.cn
fengcf@sdu.edu.cn
hyzhang@ynu.edu.cn
llma@ihep.ac.cn

Understanding the disparities in muon content of EASs is crucial for understanding the discrepancies between model predictions and observations. The Large High Altitude Air Shower Observatory (LHAASO), equipped with 1188 soil-buried MDs, provides unparalleled precision in measuring muon content. This study specifically focused on determining the attenuation length of muon content in very-high-energy EASs ranging from 0.3 to 30 PeV, which encompasses the knee region of the all-particle energy spectrum.

The remainder of this paper is organized as follows. Section II describes the experimental setup and event information for the LHAASO array, including the performance of MDs, principles of muon content measurement, generation of simulations, and event selection criteria. In Section III, the attenuation lengths of muon content were assessed using the constant intensity cut (CIC) method. Additionally, the attenuation lengths of simulated data (EPOS-LHC, QGSJET-II-04, and SIBYLL 2.3d) were measured, and the variation trends in the attenuation length with the integral flux and energy are presented. We also provide a detailed analysis of the sources of systematic errors. Finally, Section IV presents the conclusions.

II. EXPERIMENTS AND SIMULATIONS

A. LHAASO KM2A detector

LHAASO is a ground-based air shower observatory located 4410 m above sea level in Daocheng, China [6]. It contains a hybrid detector array comprising an EAS array covering an area of 1.3 km² (KM2A), 78,000 m² water Cherenkov detector array (WCDA), and 18 wide-field air Cherenkov/fluorescence telescopes (WFCTA). KM2A consists of 1188 MDs with a spacing of 30 m and 5216 electromagnetic detectors (EDs) with a spacing of 15 m; these detectors record muons and electromagnetic particles, respectively, as shown in Fig. 1.

Each ED is composed of a plastic scintillation detector with an area of 1 m² covered with a 5 mm lead plate on its surface. It absorbs low-energy charged particles from atmospheric showers and converts gamma rays into positron-electron pairs. EDs are used to detect charged particles and gamma rays in the EAS and to reconstruct the arrival directions and core positions of primary cosmic-rays.

Each MD is composed of a water Cherenkov detector with an area of 36 m². Fig. 2 shows a schematic of an MD. Each MD unit consists of a concrete tank with a diameter of 6.8 m and a depth of 1.2 m. The interior of the tank contains ultra-pure water enclosed in a highly reflective ($\geq 95\%$) bag. Additionally, there is an overburden soil layer above the MD; it is approximately 2.5 m thick and absorbs electromagnetic and other charged particles in the shower. However, muons with energies greater than 1 GeV can penetrate overburden soil [7]. Thus, an 8-inch photo-multiplier tube (PMT) is positioned at the top surface of the water [8]. It is responsible for collecting the Cherenkov light emitted by high-energy muons. The total muon-sensitive area in LHAASO exceeds 40,000 m².

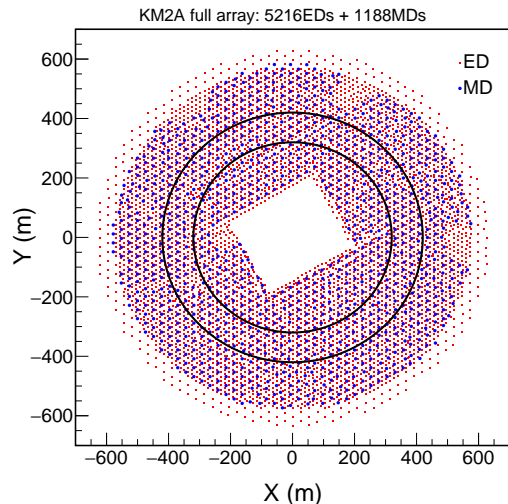


Figure 1. Layout of the KM2A full array. The red squares and blue dots indicate the EDs and MDs in operation, respectively. Showers are selected with reconstructed cores falling in the ring between the two black circles, featuring inner and outer radii of 320 and 420 m, respectively.

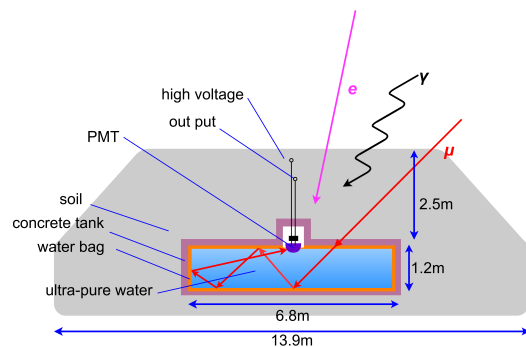


Figure 2. Schematic of LHAASO-KM2A muon detector. One water tank is buried under 2.5 m of soil. The ultra-pure water within the tank reaches a depth of 1.2 m and is enclosed in a highly reflective bag.

Moreover, owing to its wide dynamic range, the MDs can detect up to 10,000 particles, which enables accurate measurement of muon content across a broad energy range without saturation [6].

B. Muon content measurement

When one muon particle through an MD, the Cherenkov light emitted from pure water is collected by the PMT after multiple reflections within the tank. The PMT signals pass through a shaping circuit and are then continuously digitized using flash analog-to-digital converters (FADCs) [6]. When the signal amplitude of one FADC channel exceeds the preset threshold, the signal is recorded as one ‘hit’ and this MD is recorded as a fired detector. An event trigger is generated if more than 20 EDs are fired within a 400 ns time window. In this work, we restrict the arrival time of particles to within $[-30, 50]$ ns around the shower front, to suppress background or

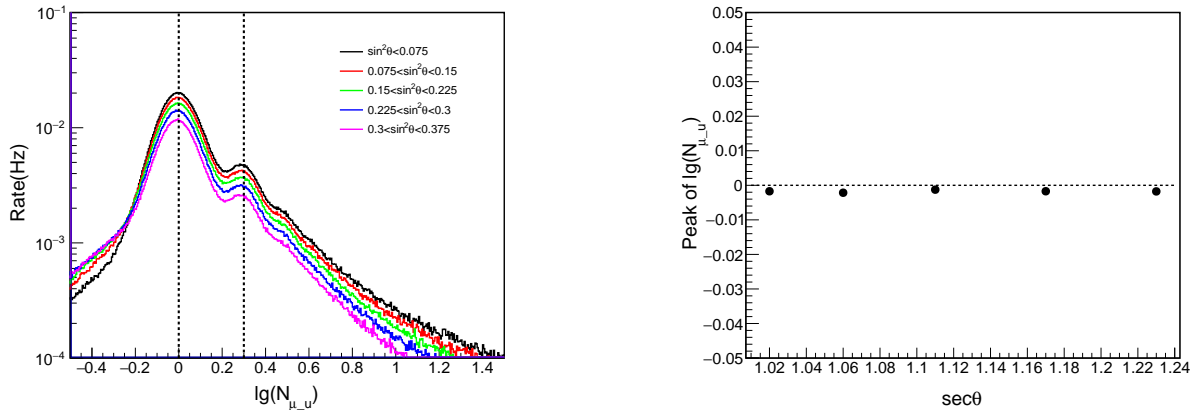


Figure 3. Left: Logarithmic number of muons distribution of one single MD unit ($N_{\mu-u}$) after zenith angle correction for each zenith angle. The vertical dash line indicates the position of the single-muon peak and double-muon peak. Right: Fitting value of the logarithmic single-muon peak for each zenith angle; the error bar is smaller than the mark size.

detector noise as doing in [9].

The total number of muons of a triggered event is the sum number of muons from all fired MDs. The number of muons of each fired MD are derived by dividing the number of photonelectrons (NPE) recorded by the MD by $VEM/\cos(\theta)$. Here VEM is the vertical equivalent muon and θ is the zenith angle of the event. The VEM of each MD is calibrated once daily by almost vertical events [10]. An inclined muon travels a longer path in the tank water of the MD compared to a vertical muon, leading to a larger NPE. The NPE produced by a single muon is proportional to the path length; therefore, the equivalent muon for inclined showers should be $VEM/\cos(\theta)$ [7]. The distribution of muons from an individual MD in different directions is shown in the left-hand panel of Fig. 3. It can be observed that the single-muon and double-muon peaks are the same for each zenith angle bin. The right-hand panel of Fig. 3 shows the peak values of single-muon at each zenith angle range more clearly, and no zenith angle dependence was observed.

The high-energy electromagnetic particles near the core of the shower can punch through the shielding soil of an MD and become recorded as muon. To reduce the punch-through effect of high-energy electromagnetic particles near the shower core, hits within 40 m from the shower axis are not counted. Hits 200 m away from the shower axis are not counted either because of the limited size of KM2A. Therefore, in this study, the number of muons recorded by MDs within a distance of 40-200 m from the shower axis in a shower event was defined as the muon content N_{μ} of a shower event. According to [11], the muon content within this 40–200 m range exhibits a strong linear relationship with the true muon content.

C. Monte Carlo simulation

Monte Carlo simulations were performed to compare the results with those obtained using interaction models. The COsmic Ray SIMulations for KASCADE (CORSIKA) code (version 7.7410) [12] software package was used to simulate EASs of cosmic-rays with primary ener-

gies ranging from 100 TeV to 100 PeV. The zenith angles of the incident cosmic-rays were sampled within 0° – 40° . In CORSIKA simulation, the low-energy hadronic interaction model Fluka [13] and high-energy hadronic interaction models QGSJET-II-04 [14], EPOS-LHC [15], and SIBYLL 2.3d [16] were employed for model validation. The number of events simulated by the QGSJET-II-04 model exceeded 7.1×10^7 , whereas the number of events simulated by EPOS-LHC and SIBYLL 2.3d exceeded 3.5×10^7 . The primary particle components in the simulation included hydrogen (H), helium (He), nitrogen (N), aluminum (Al), and iron (Fe) nuclei.

The ED and MD detector responses were simulated using the G4KM2A [17] package developed in the framework of GEANT4 [18]. Random noise in a single ED and MD was also considered in the simulation.

The simulation data were normalized according to several popular assumed energy spectra, including Gaisser H3a [19], Horandel [20], and Global Spline Fit (GSF) [21]. A new spectrum model [22] developed according to the last published LHAASO spectrum results [23] was used; in this study, it is denoted as the LHAASO spectrum. The simulation results were validated using LHAASO KM2A data, which matched well with the data [9].

The G4KM2A package, operating in single unit mode, was also used to investigate the detector's response to muon counting across different zenith angle windows. A total of 1.2 million muons were injected within a 15 m radius, with zenith angle uniformly distributed according to $\sin^2\theta$ in the range of 0° – 45° . The number of injected-muons within one zenith angle bin is denoted as M_{μ} , and the number of measured-muons within this zenith angle bin is N'_{μ} (also corrected with $VEM/\cos(\theta)$ as detector done). Fig. 4 illustrates the ratio N'_{μ}/M_{μ} for different zenith angles. The fitting results indicate the ratio remains almost constant across the zenith angle range, indicating that the detector's response to the number of muons is independent of the zenith angle of the air shower.

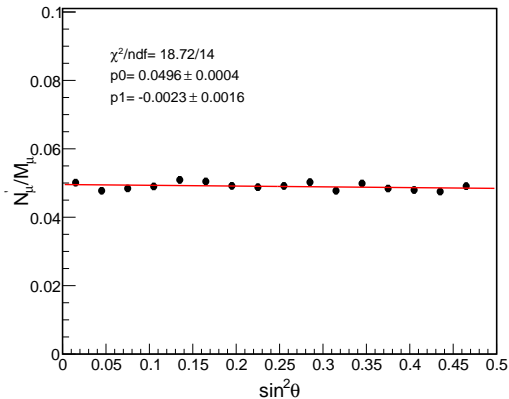


Figure 4. The distribution of the ratio between injected and measured number of muons across different zenith angles. The red line represents the result of linear fitting.

D. Data and event selection

The experimental data spanned two years, from August 2021 to July 2023, totaling 730 days. To obtain high-quality measurement results, the following event selection criteria were applied:

- (1) The electromagnetic particle number (N_e) of the shower, considering the ED within a distance of 40-200 m from the shower axis, must be greater than 80;
- (2) The distance from the shower core to the array center is within 320-420 m, as shown by the black circles in Fig. 1;
- (3) Zenith angle $\theta \leq 40^\circ$.

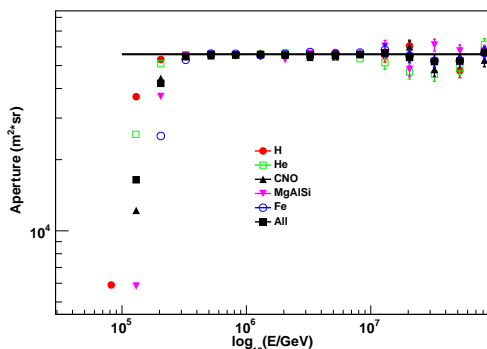


Figure 5. The aperture of the KM2A full-array for cosmic-rays varies with the primary energy of different components. The selection criteria were $N_e \geq 80$, shower core within 320-420 m, and $33.41^\circ \leq \theta \leq 38^\circ$.

The effective detection area of KM2A can be calculated using simulation data and is dependent on the energy, zenith angle, and composition. Fig. 5 shows the apertures of different components within the largest zenith angle bin in this study (between 33.41° and 38°) after event selection. The effective aperture increases with energy and reaches full efficiency for all components when

the shower energy exceeds $\lg(E/\text{GeV}) \geq 5.5$. This energy threshold also guarantees full efficiency for showers with zenith angles smaller than those shown in this plot, given that the efficiency increases with decreasing zenith angle. The subsequent analysis is based on full-efficiency measurement and requires a primary energy $\lg(E/\text{GeV}) \geq 5.5$.

The atmospheric pressure has an impact on the measurement of muon content. By utilizing the relationship between the number of muons and the atmospheric pressure, we adjusted the number of muons to that under standard atmospheric pressure. The influence of atmospheric pressure on the measurement of muon content was 4.4%, becoming 0.6% after correcting for atmospheric pressure [23].

The calibration uncertainty of one ED and MD for a single particle are less than 2% [10] and 0.5% [7], respectively. At 300 TeV, the average numbers of triggered EDs and MDs were approximately 200 and 50, respectively. Therefore, the measurement uncertainties of N_e and N_μ are both less than 0.15%. The zenith angle resolution is less than 0.2° at 400 TeV [9].

III. MEASUREMENT OF THE ATTENUATION LENGTH OF MUON CONTENT

A. Attenuation length measurement

The CIC method [24] was used to infer the attenuation length of muon content in air showers. This method is based on the assumption that the arrival distribution of cosmic-rays is isotropic; thus, the observed intensity of primary particles with the same energy is independent of the zenith angle or slant depth. This method depends on no supposed simulation models. The purpose of this study was to compare the muon content in air showers with the same primary energy at different zenith angles or different atmospheric depths.

To apply the CIC method, the data after selection were grouped into nine zenith angle intervals (zenith angle within 14.18° - 35.06° with the same aperture $\Delta \sin^2 \theta = 0.03$, shower core within 320-420 m) as shown in the left-hand panel of Fig. 6, where only five zenith angles are displayed. The integral muon flux, $J(\geq N_\mu, \theta)$ ($\text{m}^{-2} \cdot \text{s}^{-1} \cdot \text{sr}^{-1}$), was estimated based on the differential muon content spectrum using the following formula:

$$J(\geq N_\mu, \theta) = \int_{N_\mu} \Phi(N_\mu, \theta) dN_\mu, \quad (1)$$

where $\Phi(N_\mu, \theta)$ represents the differential muon content spectrum in the direction of the zenith angle θ . CICs were performed at a constant flux $J(\geq N_\mu, \theta)$ on the integral spectrum of each zenith angle θ direction within fourteen flux ranges: $\lg[J/(\text{m}^{-2} \cdot \text{s}^{-1} \cdot \text{sr}^{-1})] \in [-8.9, -5.0]$. The logarithmic muon contents of the CICs in the flux along direction θ are shown in the right-hand panel of Fig. 6 for each flux cut; only six cut values are displayed.

At each flux cut, the muon content of the air shower was attenuated as the zenith angle θ increased (with a longer atmospheric depth), as shown in the right-hand

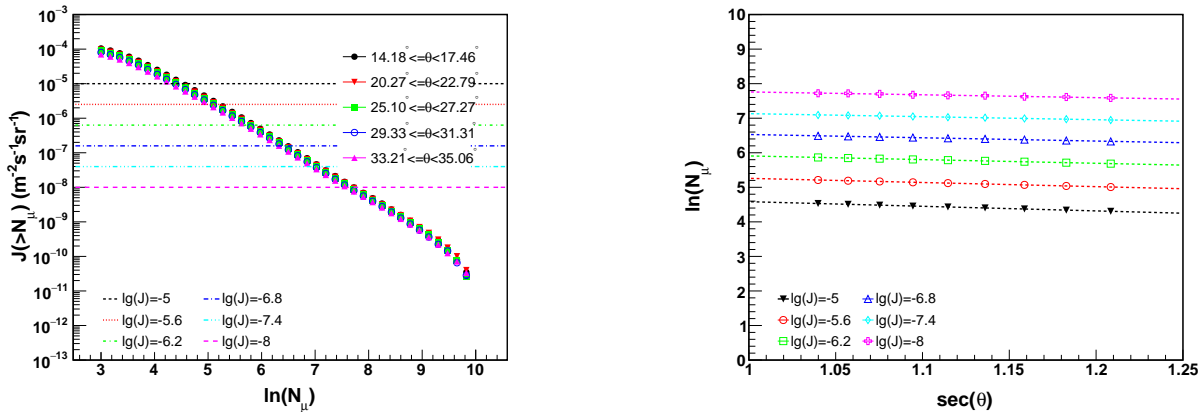


Figure 6. Left: Distribution of the integral muon flux for five zenith angle intervals with same aperture. The different marks represent the integral spectra for each zenith angle intervals. The dashed lines of six different colors represent the six cut fluxes. The statistical error bar is shorter than the mark size. Right: Logarithmic muon content distribution in terms of the zenith angle of the shower corresponding to the CIC method at one constant flux. The six different colored marks represent the variations of N_μ with zenith angle under six different cut fluxes. The error bars are smaller than the size of the marks.

panel of Fig. 6. To obtain the attenuation length of the muon content, we fit the attenuation curves using the following formula:

$$N_\mu(\theta) = N_\mu^0 e^{-\frac{X_0 \cdot \sec(\theta)}{\Lambda_\mu}}, \quad (2)$$

where $N_\mu(\theta)$ is the muon content of the shower with zenith angle θ ; N_μ^0 is the normalization parameter, which is equal to the muon content of the vertical incident-event showers; X_0 is the vertical atmospheric depth, equal to $600 \text{ g}\cdot\text{cm}^{-2}$ at LHAASO, and Λ_μ is the attenuation length of the muon content.

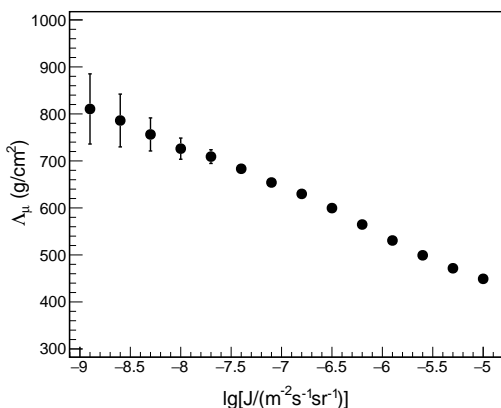


Figure 7. The attenuation length of the muon content varies with the flux cut. The bars represent statistical errors.

The attenuation length Λ_μ can be obtained by linearly fitting the relationship between the logarithmic muon content ($\ln(N_\mu)$) and zenith angle ($\sec(\theta)$) or atmospheric depth ($X_0 \cdot \sec(\theta)$). The slope of the fitted line is expressed as X_0/Λ_μ . The attenuation lengths of the muon content for different flux cuts were measured according to the fitting results, as shown in Fig. 7. The attenuation length of the muon content increased from 449 to $811 \text{ g}\cdot\text{cm}^{-2}$ for the logarithmic integral flux decreasing from -5.0 to -8.9

$\text{m}^{-2}\cdot\text{s}^{-1}\cdot\text{sr}^{-1}$. The attenuation length for each flux cut is listed in Table I together with the corresponding statistical error. These results, which constitute the baseline for the systematic error analysis presented in the next section, are independent of any supposed hadronic interaction or spectrum models.

B. Systematical errors

Atmospheric pressure variation results in fluctuations of the atmosphere depth and muon content. However, it becomes negligible after correction of the muon content with the atmospheric pressure, as discussed in part D of Section II. The measurement precision of the muon content was very high, as mentioned in that part. Therefore, the uncertainties induced by the atmospheric pressure and muon content precision were disregarded in this study.

The measured results were based on the integral flux of $\ln(N_\mu)$, and the effect of the bin size of $\ln(N_\mu)$ on the attenuation lengths was investigated. Additionally, the number of degrees of freedom during the fitting process was examined. These systematic errors were too small to be considered.

The main systematic errors were as follows:

- (1) Zenith angle interval size
- (2) Zenith angle range
- (3) Shower core range

In the baseline analysis above, events within a zenith angle range of 14.18° – 35.06° were divided into nine zenith angle intervals based on $\Delta \sin^2 \theta = 0.03$. For comparison, the zenith angle was divided into intervals with a larger aperture $\Delta \sin^2 \theta = 0.05$ and smaller aperture $\Delta \sin^2 \theta = 0.02$. The uncertainties in the measured attenuation length from the zenith angle interval size are listed in the A(zenith angle interval size)-th column of Table I for each flux cut. The uncertainties are less than 2% for flux

$\lg[J/(\text{m}^{-2}\cdot\text{s}^{-1}\cdot\text{sr}^{-1})] \geq -8.0$, and the uncertainty is larger than 10% for the last point $\lg[J/(\text{m}^{-2}\cdot\text{s}^{-1}\cdot\text{sr}^{-1})] = -8.9$, but still comparable with its statistical error.

In the baseline analysis, the range of the fitted zenith angle was 14.18° – 35.06° , corresponding to the atmospheric depth ($X_0 \cdot \sec(\theta)$) within 618 – $733 \text{ g}\cdot\text{cm}^{-2}$. We skipped the observation aperture up and down in two zenith angle ranges, namely 0° – 31.31° and 20.27° – 38.65° with equal apertures, and measured the attenuation length for the same zenith angle interval as the baseline. The uncertainties from the zenith angle range are listed in the B(zenith angle range)-th column of Table I for each flux cut. The uncertainties are similar to those caused by the size of the interval and were controlled for the flux $\lg[J/(\text{m}^{-2}\cdot\text{s}^{-1}\cdot\text{sr}^{-1})] \geq -8.3$.

In the baseline analysis, the shower core of the events was limited to 320 – 420 m from the center of the array. A wider (narrower) shower core range of 300 – 450 (350 – 400) m from the array center was selected for systematic error study. The uncertainties in the shower core selection are listed in the C(shower core range)-th column of Table I for each flux cut. The uncertainties were almost the same for all fluxes except for the last one. According to Table I, the shower core is the dominant uncertainty for a larger flux but is equal to the above two systematic uncertainties when the flux $\lg[J/(\text{m}^{-2}\cdot\text{s}^{-1}\cdot\text{sr}^{-1})] \leq -8.6$.

The last column in Table I lists the total systematic errors for each flux cut. The total systematic errors were less than 6% except for the last two flux cuts ($\lg[J/(\text{m}^{-2}\cdot\text{s}^{-1}\cdot\text{sr}^{-1})] \geq -8.6$). The total systematic errors were larger than the statistical errors for all the flux cuts.

C. Comparison of experimental and simulated attenuation lengths

The LHAASO Collaboration has recently published the most accurate all-particle differential energy spectrum within the energy range of 0.3 – 30 PeV [23]. The all-particle energy spectrum of LHAASO fitted well with the following formula:

$$J(E) = \Phi_0 \cdot (E)^{\gamma_1} \left(1 + \left(\frac{E}{E_b} \right)^s \right)^{(\gamma_2 - \gamma_1)/s}, \quad (3)$$

where $E_b = 3.67 \text{ PeV}$ corresponds to the knee position, $\gamma_1 = -2.7413$ and $\gamma_2 = -3.128$ are the slopes of the energy spectrum below and above the knee, and $s = 4.2$ is the sharpness of the knee.

By integrating this spectrum, the corresponding shower energy of each cosmic-ray flux was estimated and listed in the second column of Table I. The uncertainty of this estimated energy is less than 3% according to the uncertainty of the published energy spectrum, which includes the systematic error from the interaction models, composition models, and atmospheric pressure.

Therefore, the flux is transferred to cosmic-ray energy according to Table I, and the variation in the attenuation length with shower energy is shown by the black dots in Fig. 8. The attenuation lengths of the muon content increase with the cosmic-ray energy. The systematic error

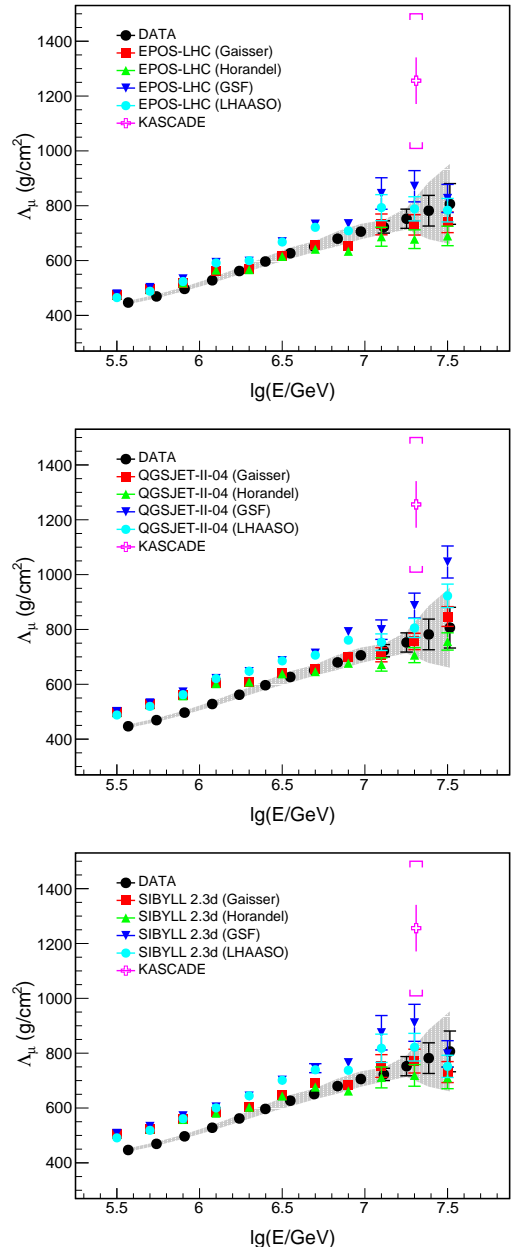


Figure 8. The muon content attenuation length varies with the cosmic-ray energy. The measured results with LHAASO data are represented by black dots. The error bars represent the statistical error whereas the gray shadow represents the systematic error. The error bar of the energy is shorter than the dot size. The attenuation lengths are plotted according to the simulation data produced with the hadronic interaction models EPOS-LHC (upper panel), QGSJET-II-04 (middle panel), and SIBYLL 2.3d (down panel), after normalization with spectrum models. Only the statistical errors are shown for the simulation results. The red square, green up triangle, and blue down triangle represent the attenuation length of the muon content for the spectrum models of the Gaisser H3a [19], Horandel [20], and GSF [21] models, and the azure dots represent the results from the LHAASO spectrum model, which was developed based on the all-particle energy spectrum [22] measurement of LHAASO. The pink cross represents the attenuation length of the KASCADE results [5] with energy ranging from 20 to 100 PeV.

is also shown as a shadow in this figure, according to the total systematic error shown in Table I.

To validate the interaction models with our measured results, cosmic-ray air showers were simulated using three hadronic interaction models. The simulation data were normalized based on four energy spectrum models, as described in part C of Section II. Utilizing these normalized cosmic-ray air shower simulation data, the attenuation lengths of the muon content were re-evaluated by fitting the variation in muon content with the zenith angle for each shower energy bin, similar to the data. The simulation results are plotted together with results from LHAASO data in Fig. 8 to compare the events with equal energy for three hadronic interaction models: EPOS-LHC, QGSJET-II-04, and SIBYLL 2.3d. The results of four energy spectrum models (Gaisser H3a, Horandel, GSF, and LHAASO) were compared for each interaction model.

The increasing trend in the attenuation lengths of the muon content with the cosmic-ray energy was confirmed by the simulation results for the three hadronic interaction models, as shown at the top, middle, and bottom panels of Fig. 8. The attenuation lengths of the simulation data for both QGSJET-II-04 and SIBYLL 2.3d models were significantly longer than those of the LHAASO data, as shown in the middle and bottom panels of Fig. 8. The results of the EPOS-LHC model were closer to the experimental data than those of the other models, as shown in the top panel of Fig. 8. In future analyses, we will continue to study the variations according to different hadronic models relative to energy.

The attenuation lengths obtained from the LHAASO data were shorter than those obtained from the simulation data, which were normalized to the LHAASO energy spectrum over the entire energy range. The results for the GSF energy spectrum were similar to those of the LHAASO energy spectrum. However, the attenuation lengths of the Gaisser H3a and Horandel energy spectra were shorter than those of the LHAASO and GSF spectra above 2 PeV, where the mean mass of the Gaisser H3a and Horandel models is heavier than that of the data [23].

The KASCADE-Grande Collaboration measured the attenuation length of the muon content for cosmic-ray air showers within 20-100 PeV at sea level. In particular, the muon content was measured by fitting the lateral distribution with a Lagutin-Raikin function with fixed shape. The attenuation length was $1256 \pm 85_{-232}^{+229}$ g·cm⁻², which is longer than the results from simulation data [5]. The results from LHAASO data with similar energy were shorter than that from KASCADE data, as shown in Fig. 8, but close to the simulation results.

IV. CONCLUSION

LHAASO KM2A has measured electromagnetic particles and muons with very high precision for cosmic-ray air showers with energy between 0.3-30 PeV, where the

cosmic-ray energy spectrum becomes steeper. By using the data collected by LHAASO-KM2A within two years, from August 2021 to July 2023, the attenuation lengths of the muon content for cosmic-ray air showers with energy between 0.3 to 30 PeV were measured using the CIC method. The attenuation length increased from 449 to 811 g·cm⁻² as the shower energy increased from 0.3 to 30 PeV. These results are independent of the proposed models.

The air shower simulations were performed using three hadronic interaction models, namely EPOS-LHC, QGSJET-II-04, and SIBYLL 2.3d, and were normalized according to four energy spectra, including one LHAASO energy spectrum. The simulation results confirmed an increasing trend in the attenuation length of the muon content with the shower energy. The attenuation lengths of the QGSJET-II-04 and SIBYLL 2.3d models were longer than those of the LHAASO data, and the results of EPOS-LHC were relatively close to the LHAASO data. The LHAASO results are more suitable for the EPOS-LHC model than for the other two models.

V. ACKNOWLEDGMENTS

We would like to thank all staff members who work at the LHAASO site 4400 m above sea level year-round to maintain the detector and water recycling system, electricity power supply, and other components of the experiment operating smoothly. We are grateful to the Chengdu Management Committee of Tianfu New Area for their constant financial support for research using the LHAASO data. We appreciate the computing and data service support provided by the National High Energy Physics Data Center for the data analysis. This research study was supported by the following grants: National Natural Science Foundation of China (Nos.12175121, 12275280, 12393851, 12393852, 12393853, 12393854, 12205314, 12105301, 12305120, 12261160362, 12105294, U1931201, and 12375107, Thailand by the National Science and Technology Development Agency (NSTDA), and the National Research Council of Thailand (NRCT) under the High-Potential Research Team Grant Program (N42A650868).

VI. AUTHOR CONTRIBUTIONS

X.T. Feng led the drafting of the manuscript and analyzed the data. H.Y. Zhang played a pivotal role in cross-checking, preparing the simulation data, and revising the manuscript. L.L. Ma and C.F. Feng, as co-proponents, provided guidance for data analysis and manuscript revision. Z. Cao is the spokesperson for the LHAASO Collaboration and principal investigator of the LHAASO project. All other authors participated in data analysis, including detector calibration, data processing, event reconstruction, data quality check, and various simulations, and provided comments on the manuscript.

Table I. List of attenuation lengths of the muon content for each flux (shower energy) with systematical and statistical errors; the A-th column represents the zenith angle interval size, the B-th column represents the zenith angle range, and the C-th column represents the shower core range.

$\lg[J/(\text{m}^{-2}\cdot\text{s}^{-1}\cdot\text{sr}^{-1})]$	$\lg[E_{rec}/(\text{GeV})]$	$\Lambda_{\mu} \pm \text{Stat} \pm \text{Syst} (\text{g}\cdot\text{cm}^{-2})$	A(%)	B(%)	C(%)	Stat(%)	Syst(%)
-5.0	5.57	449.1±0.3±6.7	0.1	0.6	1.3	0.1	1.5
-5.3	5.74	471.6±0.4±7.1	0.2	0.4	1.4	0.1	1.5
-5.6	5.91	499.2±0.7±8.0	0.4	0.4	1.5	0.2	1.6
-5.9	6.08	530.7±1.1±10.1	0.6	0.8	1.6	0.2	1.9
-6.2	6.24	564.7±1.7±15.8	0.8	1.3	1.8	0.3	2.3
-6.5	6.40	599.6±2.6±16.8	1.1	1.8	1.8	0.5	2.8
-6.8	6.55	629.9±4.0±21.4	1.9	2.2	1.8	0.7	3.4
-7.1	6.69	654.1±6.0±20.3	1.1	2.3	1.8	1.0	3.1
-7.4	6.84	683.3±9.2±28.0	1.9	2.6	2.6	1.4	4.1
-7.7	6.98	709.2±14.6±29.1	1.7	2.1	3.0	2.1	4.1
-8.0	7.11	726.1±22.5±26.1	1.7	2.1	2.4	3.1	3.6
-8.3	7.25	756.3±35.2±40.1	3.6	3.3	2.1	4.7	5.3
-8.6	7.39	786.0±56.2±110.0	7.0	11	3.4	7.2	14
-8.9	7.51	810.6±74.6±153.9	12	12	7.5	9.2	19

- [1] A. Aab *et al.* (Pierre Auger Collaboration), Testing hadronic interactions at ultrahigh energies with air showers measured by the pierre auger observatory, *Phys. Rev. Lett.* **117**, 192001 (2016).
- [2] R. U. Abbasi, M. Abe, T. Abu-Zayyad, *et al.* (Telescope Array Collaboration), Study of muons from ultrahigh energy cosmic ray air showers measured with the telescope array experiment, *Phys. Rev. D* **98**, 022002 (2018).
- [3] J. A. Bellido, R. W. Clay, *et al.*, Muon content of extensive air showers: Comparison of the energy spectra obtained by the sydney university giant air-shower recorder and by the pierre auger observatory, *Phys. Rev. D* **98**, 023014 (2018).
- [4] R. Abbasi, M. Ackermann, *et al.* (IceCube Collaboration), Density of gev muons in air showers measured with icetop, *Phys. Rev. D* **106**, 032010 (2022).
- [5] W. Apel, J. Arteaga-Velázquez, *et al.*, Probing the evolution of the eas muon content in the atmosphere with kascade-grande, *Astroparticle Physics* **95**, 25 (2017).
- [6] H. He, Design of the lhaaso detectors, *Radiation Detection Technology and Methods* **2**, 10.1007/s41605-018-0037-3 (2018).
- [7] X. Zuo, G. Xiao, *et al.*, Design and performances of prototype muon detectors of lhaaso-km2a, *Nuclear Instruments and Methods in Physics Research Section A: Accelerators, Spectrometers, Detectors and Associated Equipment* **789**, 143 (2015).
- [8] Y. Yu, H. Lv, X. Sheng, D. Liu, and C. Feng, Performance test and qualification of the photomultiplier tube for the whole production of lhaaso-ed, *Nuclear Instruments and Methods in Physics Research Section A: Accelerators, Spectrometers, Detectors and Associated Equipment* **1025**, 166120 (2022).
- [9] F. Aharonian, Q. An, *et al.*, Observation of the crab nebula with LHAASO-KM2A - a performance study, *Chinese Physics C* **45**, 025002 (2021).
- [10] F. Aharonian, Q. An, *et al.* (LHAASO Collaboration), Self-calibration of lhaaso-km2a electromagnetic particle detectors using single particles within extensive air showers, *Phys. Rev. D* **106**, 122004 (2022).
- [11] H. Zhang, H. He, and C. Feng, Approaches to composition independent energy reconstruction of cosmic rays based on the lhaaso-km2a detector, *Phys. Rev. D* **106**, 123028 (2022).
- [12] D. Heck, J. Knapp, *et al.*, *CORSIKA: A Monte Carlo code to simulate extensive air showers*, Tech. Rep. (1998) fZKA-6019 (Februar 98).
- [13] G. Battistoni, T. Boehlen, *et al.*, Overview of the fluka code, *Annals of Nuclear Energy* **82**, 10 (2015).
- [14] S. Ostapchenko, Monte carlo treatment of hadronic interactions in enhanced pomeron scheme: Qgsjet-ii model, *Phys. Rev. D* **83**, 014018 (2011).
- [15] T. Pierog, I. Karpenko, J. M. Katzy, E. Yatsenko, and K. Werner, Epos lhc: Test of collective hadronization with data measured at the cern large hadron collider, *Phys. Rev. C* **92**, 034906 (2015).
- [16] F. Riehn, R. Engel, A. Fedynitch, T. K. Gaisser, and T. Stanev, Hadronic interaction model sibyll 2.3d and extensive air showers, *Phys. Rev. D* **102**, 063002 (2020).
- [17] Z. Cao, F. Aharonian, *et al.*, Lhaaso-km2a detector simulation using geant4, *Radiation Detection Technology and Methods* 10.1007/s41605-024-00467-8 (2024).
- [18] S. Agostinelli, J. Allison, *et al.*, Geant4—a simulation toolkit, *Nuclear Instruments and Methods in Physics Research Section A: Accelerators, Spectrometers, Detectors and Associated Equipment* **506**, 250 (2003).
- [19] T. Gaisser, T. Stanev, and S. Tilav, Cosmic ray energy spectrum from measurements of air showers, *Frontiers of Physics* 10.1007/s11467-013-0319-7 (2013).
- [20] J. R. Hörandel, On the knee in the energy spectrum of cosmic rays, *Astroparticle Physics* **19**, 193 (2003).
- [21] H. Dembinski *et al.*, Data-driven model of the cosmic-ray flux and mass composition from 10 GeV to 10^{11} GeV, *Proc. Sci. ICRC2017*, 533 (2017).
- [22] X.-J. Lv, X.-J. Bi, K. Fang, Y.-Q. Guo, H.-H. He, L.-L. Ma, P.-F. Yin, Q. Yuan, and M.-J. Zhao, Precise measurement of the cosmic-ray spectrum and $\langle \ln a \rangle$ by lhaaso – connecting the galactic to the extragalactic components (2024), [arXiv:2403.11832 \[astro-ph.HE\]](https://arxiv.org/abs/2403.11832).
- [23] Z. Cao, F. Aharonian, *et al.* (LHAASO Collaboration), Measurements of all-particle energy spectrum and mean logarithmic mass of cosmic rays from 0.3 to 30 pev with lhaaso-km2a, *Phys. Rev. Lett.* **132**, 131002 (2024).
- [24] C. J. Bell, A. D. Bray, *et al.*, The upper end of the observed cosmic ray energy spectrum, *Journal of Physics A: Mathematical, Nuclear and General* **7**, 990 (1974).